K+-Doped Li$_{1.2}Mn_{0.54}Co_{0.13}Ni_{0.13}O_2$: A Novel Cathode Material with an Enhanced Cycling Stability for Lithium-Ion Batteries

Qi Li,[†] Guangshe Li,[†] Chaochao Fu,[‡] Dong Luo,[‡] Jianming Fan,[‡] and Liping Li*[,‡]

[†]State Key Laboratory of Structural Chemistry, Fujian Institute of Research on the Structure of Matter, University of Chinese Academy of Sciences, Fuzhou 350002, P. R. China

[‡]Key Lab of Optoelectronic Materials Chemistry and Physics, Fujian Institute of Research on the Structure of Matter, University of Chinese Academy of Sciences, Fuzhou, 350002, P. R. China

Ⓢ Supporting Information

ABSTRACT: Li-rich layered oxides have attracted much attention for their potential application as cathode materials in lithium ion batteries, but still suffer from inferior cycling stability and fast voltage decay during cycling. How to eliminate the detrimental spinel growth is highly challenging in this regard. Herein, in situ K+-doped Li$_{1.20}$Mn$_{0.54}$Co$_{0.13}$Ni$_{0.13}$O$_2$ was successfully prepared using a potassium containing α-MnO$_2$ as the starting material. A systematic investigation demonstrates for the first time, that the in situ potassium doping stabilizes the host layered structure by prohibiting the formation of spinel structure during cycling. This is likely due to the fact that potassium ions in the lithium layer could weaken the formation of trivacancies in lithium layer and Mn migration to form spinel structure, and that the large ionic radius of potassium could possibly aggravate steric hindrance for spinel growth. Consequently, the obtained oxides exhibited a superior cycling stability with 85% of initial capacity (315 mA h g^{-1}) even after 110 cycles. The results reported in this work are fundamentally important, which could provide a vital hint for inhibiting the undesired layered-spinel intergrowth with alkali ion doping and might be extended to other classes of layered oxides for excellent cycling performance.

KEYWORDS: K+-doping, lithium ion batteries, Li-rich layered oxides, phase transition, cycling stability
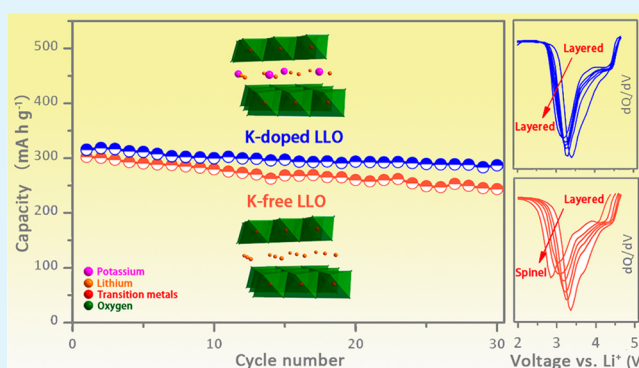
1. INTRODUCTION

A novel class of layered insertion oxides with lithium content larger than stoichiometric amount has been recently proposed.[1−4] These Li-rich oxide materials are formulated as xLi$_2$MnO$_3$·$(1-x)$LMO$_2$ (M = Mn, Co, Ni, Fe, etc.), which are constructed by an integrated layered−layered structure between Li$_2$MnO$_3$ and LMO$_2$ component in close packed oxygen skeleton. Many latest investigations indicate that these Li-rich oxides can be the highly promising cathode materials for advanced lithium-ion batteries with potential uses in all electric vehicles because of their extremely high energy density.[2,4−12] In addition, these Li-rich oxides are cheaper and more environmentally benign than commercial LiCoO$_2$, and are thus expected to find wide applications.

Despite these merits, Li-rich layered oxides (LLOs) always suffer from the inferior cycling stability, which hinder their applications.[13−15] Structural instability of xLi$_2$MnO$_3$·$(1-x)$LMO$_2$ is the intrinsic reason for the poor cycling performance. For example, an undesired spinel growth in the layered host structure usually occurs during the long-term cycling, which leads to the appearance of a ~3.0 V plateau as widely observed. This layered-spinel intergrowth is regarded as an important factor responsible for the fast capacity fading and

voltage decay upon cycling, which could also significantly lower the energy density of the whole battery.[4,5,13,14,16−23] Consequently, inhibiting the spinel growth is an effective approach to enhance the cycling stability of Li-rich oxides, which is, however, highly challenging.

Understanding the origin of spinel formation at atomic level would be beneficial for finding a suitable route to solve such a challenging problem. The emergence of spinel variant could be understood by well examining the layered structure of LiMO$_2$: the transition from layered to spinel structure requires rearrangement of transition metal ions only. Namely, one in fourth transition metals in the layered structure migrates from octahedral sites (M layer, 3b sites) to the tetrahedral sites (Li layer, 6c sites) without changing the oxygen host.[24] Although the rearrangement of transition metal ions, as observed by TEM techniques,[14,16] satisfies the thermodynamic requirement, a kinetic triggering is necessary. For example, a theoretical simulation predicts that the formation of a Li$_{tet}$-V(TM)$_{Li}$-Li$_{tet}$ dumbbell structure facilitates the migration of transition metal

ions to the lithium layer to form a 3 V spinel phase.[16] Thus, transition-metal-ion migration is sensitive to the local atomic distribution of target site, and doping foreign ions into the pristine layered structure may block the kinetically favorable path.

It was recently reported that Na doping in Li-rich oxides can inhibit the spinel growth:[25,26] Na-doped $Li_{1.20}Mn_{0.54}Co_{0.13}Ni_{0.13}O_2$ does not give impurity diffraction peaks in its ex situ XRD pattern, but those characteristic spinel peaks appear for the parent compounds. Moreover, the capacity retention over 100 cycles is raised from 79 to 89% by Na^+ doping.[25] Ates et al.[26] also draw the similar conclusion by investigating the influence of sodium doping on spinel growth with various characterizations. On the basis of the variations of Na content in the cathode material after charging, part of Na^+ incorporated in the layered structure are suggested to exchange with Li^+ in the electrolyte upon charging, thus leaving some vacancies in lithium layer. Further, they speculated that Ni^{3+} might migrate to these vacancies to protect layered structure against conversion to spinel structure. Although this speculation seems to be reasonable, the formation of Na vacancies is still questionable, because the variation of Na content was not detected in ref 25.

Potassium ($[Ar]4s^1$) has an identical outer shell with sodium ($[Ne]3s^1$), and naturally both potassium and sodium elements exhibit similar preferrences for chemical environment. However, comparing to sodium, potassium has a larger ionic radius and lower electronegativity. Therefore, K^+ ions could have a different ability of migration and/or ion exchange. More importantly, local atom envrionment between Na^+- and K^+-doped samples may also differ from each other to some extent. Then, could the similar inhibition of phase transition from layered to spinel structure occur for K^+-doped cathodes? If so, what is the main reason? To answer these questions, it is very important to study potassium doping in Li-rich oxides, which could help us to better understand the inhibiting mechanism and also offer a reference for dispeling the above-mentioned controversy regarding the variation of Na contents. In the present work, K^+-doped Li-rich layered oxides were prepared to show a stable recyclability. To comprehend the excellent cycling stability, we conducted systematic sample characterizations to examine the potassium doping effect on mitigating layered-spinel intergrowth.

2. EXPERIMENTAL SECTION

2.1. Sample Syntheses. *Precursor of Potassium-Doped α-MnO₂.* The precursor was prepared by a facile hydrothermal method.[27] Briefly, 3 mmol of $KMnO_4$ and 5 mmol of $MnSO_4 \cdot H_2O$ were mixed under vigorous stirring in 15 mL of water that contained 1 mL of concentrated H_2SO_4 for 15 min. The precursor solution was then sealed in a 20 mL Teflon-lined stainless autoclave and maintained at 160 °C for 20 min. The resulting precipitate was washed several times with deionized water and dried at 80 °C for 5 h in air. The general reaction equation could be described as follows

$$2KMnO_4 + 3MnSO_4 + 2H_2O = 5MnO_2 + 2H_2SO_4 + K_2SO_4$$
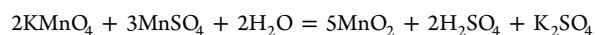
Potassium-Doped Layered Li-Rich Oxides. Stoichiometric amounts of K^+-doped $α$-MnO₂, $Ni(NO_3)_2 \cdot 6H_2O$, $Co(NO_3)_2 \cdot 6H_2O$, and $LiOH \cdot H_2O$ were mixed thoroughly. The obtained mixture was first sintered at 500 °C for 5 h; then at 800, 850, 900, or 950 °C for 12 h; and finally quenched to room temperature. The corresponding products were named as K800, K850, K900, and K950, respectively.

For comparison, potassium-free oxide was prepared using another type of $α$-MnO₂, which contains NH_4^+ in the tunnel rather than K^+. In a typical procedure,[28] 10 mmol $(NH_4)_2S_2O_8$, 6.8 mmol $MnSO_4 \cdot H_2O$

and 50 mmol $(NH_4)_2SO_4$ were first mixed in 25 mL H_2O to form a homogeneous suspension. After being dispersed by successive ultrasonication and magnetic stirring for 15 min, respectively, the suspension was transferred to a 30 mL Teflon-lined stainless steel autoclave and maintained at 180 °C for 12 h, in terms of the following reactions

$$(NH_4)_2S_2O_8 + MnSO_4 + 2H_2O$$
$$= MnO_2 + (NH_4)_2SO_4 + 2H_2SO_4$$
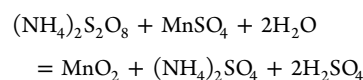
The resulting brown precipitate gave the product of $α$-MnO₂:NH_4^+. The potassium-free sample (named as N900) was obtained by sintering the mixture of $α$-MnO₂:NH_4^+ $Ni(NO_3)_2 \cdot 6H_2O$, $Co(NO_3)_2 \cdot 6H_2O$, and $LiOH \cdot H_2O$ at 900 °C for 12 h.

2.2. Sample Characterization. Powder X-ray diffraction (XRD) was executed on a Rigaku Miniflex apparatus (Cu $K\alpha$, $\lambda = 1.5418$ Å) to characterize the structure of the samples. Structural refinement was performed using General Structure Analysis System (GSAS).[29] KCl was chosen as the internal standard for peak positions calibration. Particle morphologies of the prepared samples were observed by field-emission scanning electron microscopy (SEM) (JEOL, model JSM-6700). Chemical compositions of the samples were analyzed by inductively coupled plasma atomic emission spectrometry (ICP-AES) with a relative error of ±2%. Thermogravimetric (TG) analysis and differential thermal analysis (DTA) were carried out on Netzsch Model STA449F3 thermal analyzer at a heating rate of 10 °C min⁻¹ in flowing air from room temperature to 1200 °C. The valence states of manganese, cobalt, nickel and potassium were examined by X-ray photoelectron spectroscopy (XPS) on an ESCA-LAB MKII apparatus performed with a monochromatic Al $K\alpha$ X-ray source. The charging shift was calibrated using the C 1s photoemission line at binding energy 284.8 eV.

2.3. Electrochemical Tests. Electrochemical measurements were made using CR-2025 coin cells comprising layered Li-rich oxide cathode, Li metal anode and a polymer separator (Celgard 2500) with 1 M $LiPF_6$ in EC:EMC:DMC (1:1:1 in volume) as electrolyte. The cells were assembled in an argon-filled glovebox. For fabrication of the cathodes, the prepared powders, carbon black (super P Li, Timcal) and polyvinylidene fluoride (PVDF, Alfa Aesar) binder (80:10:10, weight ratio) were mixed in N-methyl-2-pyrrolidone (NMP, Alfa Aesar). The obtained slurry was casted on aluminum foil and dried in vacuum at 100 °C overnight. The foil was then pressed and cut into disks prior to use.

Electrochemical tests were performed using Neware Test System by cycling the coin cells galvanostatically at room temperature (30 °C) between voltage limits, i.e., 2.0−4.8 V. The electrochemical impedance spectroscopy (EIS) was measured on an electrochemical workstation (CHI660C) with the applied frequency from 100 kHz to 10 MHz.

3. RESULTS AND DISCUSSION

3.1. Synthesis, Structure, and Electrochemical Performances of As-Prepared LLOs. Li-rich layered oxides were synthesized by calcining a mixture of $Ni(NO_3)_2 \cdot 6H_2O$, $Co(NO_3)_2 \cdot 6H_2O$, $LiOH \cdot H_2O$, and manganese oxide precursors generated from hydrothermal conditions. XRD and SEM measurements demonstrate that these MnO_2 precursors crystallized in a cryptomelane structure showing a morphology of nanorods with diameter of ca. 30 nm (see Figure S1a in the Supporting Information). To optimize the calcination temperature, we examined the thermal behavior of the precursor by TG - DTA. On the basis of the TG-DTA data (see Figure S1b in the Supporting Information), three temperature points of 850, 900, and 950 °C were selected as the sintering temperatures to map the samples for optimized electrochemical performance.

XRD patterns of K850, K900 and K950 samples are illustrated in Figure 1. It is obvious that all diffraction peaks
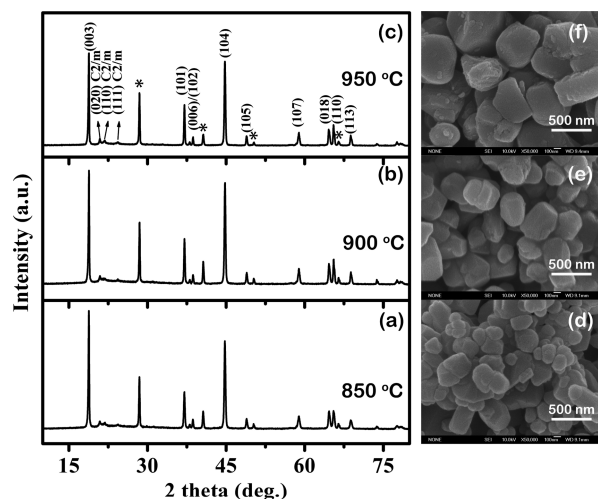
Figure 1. XRD patterns and SEM images of the samples synthesized at (a, d) 850, (b, e) 900, and (c, f) 950 °C, respectively. Miller indices for the layered structure with space group $R\bar{3}m$ and Li_2MnO_3 with $C2/m$ are given. Symbol "*" donates the internal standard of KCl.

can be readily indexed as O3 type layered structure (space group $R\bar{3}m$) except for the additional weak peaks observed between 20 and 25° (2θ), which are characteristic of Li_2MnO_3 component (space group $C2/m$).[2] Complete splitting of the pair reflections (006)/(102) and (018)/(110) indicates the formation of a typical layered structure for all samples.[8] In addition, from SEM images in Figure 1d−f, one can see that the particle sizes increased with calcination temperature from 850 to 950 °C.

Initial charge−discharge curves at a rate of 20 mA g^{-1} for samples K850, K900 and K950 are compared in Figure 2a. Clearly, all profiles displayed a smooth voltage ramp in the range between 3.7 and 4.4 V along with a plateau in the range of 4.4−4.5 V, and a small slope when charged above 4.5 V. The smooth voltage ramp could be ascribed to Li$^+$ deintercalation from the layered structure, while the long plateau could be attributed to the oxygen loss process from Li_2MnO_3

component which led to a large initial irreversible capacity loss.[7,8] The obtained samples K850, K900, and K950 delivered large discharge capacities of 238, 315, and 269 mA h g^{-1}, respectively, with an initial Coulombic efficiency of 70%, 77%, and 75%. According to the theoretical calculation,[30] $Li_{1.20}Mn_{0.54}Co_{0.13}Ni_{0.13}O_2$ could deliver the charge/discharge capacities of 378 mA h g^{-1}/252 mA h g^{-1}, respectively. It is surprising that our samples exhibited an extraordinarily higher capacity than theoretical values. The abnormally high charge capacity is possibly due to the side reactions that involve (i) electrolyte decomposition, (ii) oxidation of O^{2-} to O$^-$ or O$_2$, (iii) oxidation of Mn^{4+} to Mn^{5+}, (iv) the exchange of Li$^+$ by H$^+$, and (v) oxygen deficiencies. Meanwhile, the reversible discharge capacity >252 mA h g^{-1} implies that more than one Li could be reversibly reinserted in the host structure, as indicated by ICP analyses of K900 after first cycle (see Table 1), in agreement with the reports in refs 25 and 31. The deviation from the theoretical value could be due to the oxygen vacancies (originating from the activation of Li_2MnO_3) along with Li vacancies that are not vanished at the initial cycle. Thus, more than one Li could be reinserted to release more capacity than the theoretical value.

Rate capabilities and cycling performances at different current densities of 20−1000 mA g^{-1} for samples K850, K900, and K950 are displayed in Figure 2b−d. The almost overlapped profiles imply excellent rate capabilities for these samples. At a low rate of 20 mA g^{-1}, capacity retentions after 30 cycles for K850, K900, and K950 are 93, 91, and 98%, respectively. In fact, at higher rates, capacity retentions for each sample still remained more than 90%. Therefore, it is not just the case for a certain sample. Instead, all the Li-rich oxides prepared from the precursor α-MnO$_2$ have considerable cycling stability.

Further, sample K900 with the highest reversible capacities was selected for long-term cycling test at current densities of 20 and 400 mA g^{-1}, respectively. Corresponding profiles are shown in Figure 3. After 110 cycles, the discharge capacity at 20 mA g^{-1} approached as high as 267 mA h g^{-1} with a capacity retention of 85% relative to the first cycle. Even at a larger
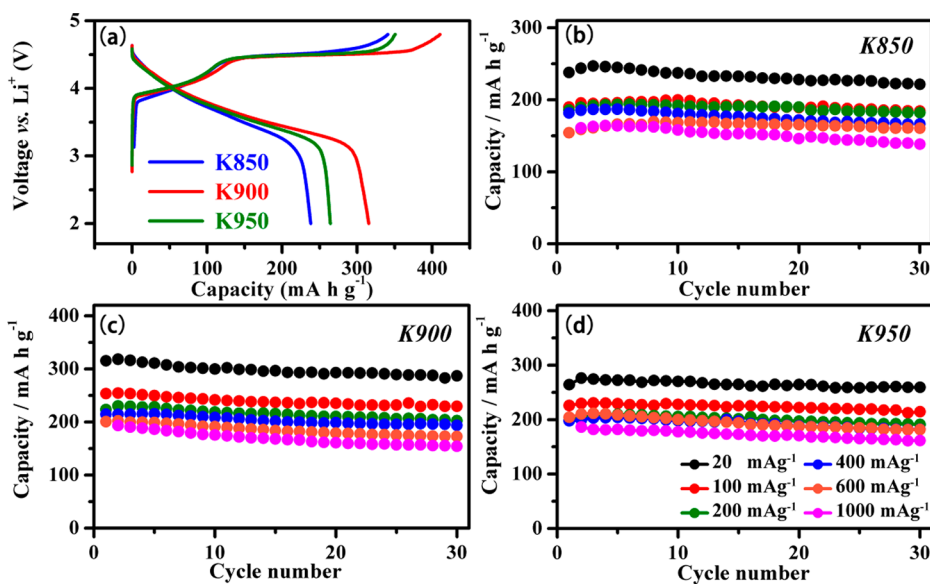

Figure 2. (a) Initial charge−discharge profiles at a current density of 20 mA g^{-1} for given samples; and cycling performances of the samples: (b) K850, (c) K900, and (d) K950 at different current densities between 20 and 1000 mA g^{-1}.

Table 1. Crystallographic Formula and Refined Lattice Parameters for $R\bar{3}m$ Phase[a]

| | crystallographic formula[b] | lattice parameters | | | | S_{MO2} (Å)[c] | I_{LiO2} (Å)[c] |
		a (Å)	c (Å)	V (Å³)	c/a		
pristine N900	$Li_{1.163}Mn_{0.560}Co_{0.140}Ni_{0.138}O_2$	2.85193(6)	14.2341(5)	100.262(5)	4.991	2.1281	2.6166
pristine K900	$Li_{1.151}K_{0.013}Mn_{0.552}Co_{0.146}Ni_{0.145}O_2$	2.85090(5)	14.2280(5)	100.147(5)	4.991	2.1114	2.6313
K900 after 1st cycle	$Li_{1.141}K_{0.013}Mn_{0.563}Co_{0.147}Ni_{0.149}O_2$						

[a]Refined parameters for $C2/m$ are provided in Table S2 in the Supporting Information. [b]The formula is calculated based on ICP results. [c]Interslab thickness is calculated according to refs 30 and 46. $I_{LiO2} = c/3 - S_{MO2}$; slab thickness $S_{MO2} = (2/3 - 2z_{ox})c$; z_{ox} is the oxygen position at 6c sites.
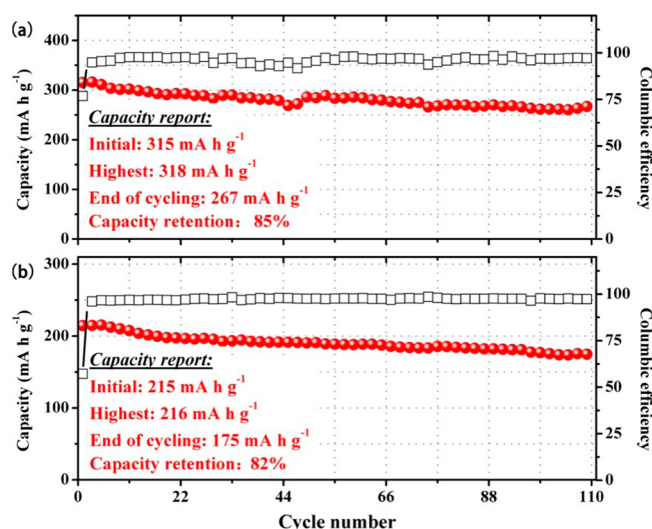

Figure 3. Cycling performance of the sample K900 at current densities: (a) 20 and (b) 400 mA g^{-1}.

current density of 400 mA g^{-1}, it still retained at 82% of the initial capacity (215 mA h g^{-1}).

Undoubtedly, LLOs prepared with α-MnO$_2$ as starting material have shown a superior cycling performance. This prompts us to perform several experiments to understand the excellent electrochemical performances of these Li-rich oxides.

First of all, it should be noted that α-MnO$_2$ has a hollandite-type structure containing one-dimensional (2 × 2) tunnels that accommodate large cations such as Na$^+$, K$^+$, NH$_4^+$, Ba^{2+}, Pb^{2+}, etc.[32,33] In this work, α-MnO$_2$ was obtained through the reduction of KMnO$_4$ in liquid, so a small amount of potassium would naturally reside in the tunnels. In the subsequent calcination steps, potassium could be in situ doped into LLOs. This is confirmed by both ICP and XPS measurements (see Table 1 and Figure 5). As a foreign component, the existence of potassium may play a key role in electrochemical performances. To make this point more clear, potassium-free samples could be a suitable reference to further understand the effect of potassium ions on the cycling performance. For comparison, a potassium-free α-MnO$_2$ in the same phase (see Figure S7 in the Supporting Information) was also synthesized and used as the starting material to prepare Li-rich layered oxides.

3.2. Influence of Potassium's Incorporation. By comparing the initial charge/discharge profiles of samples K900 and N900, it could be found that both samples delivered
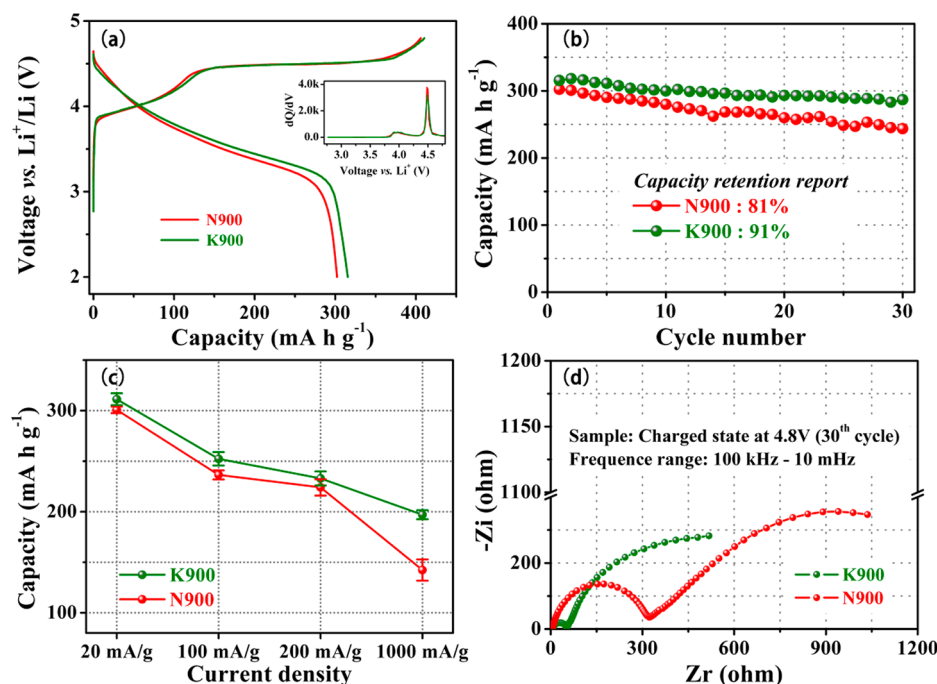

Figure 4. Comparisons of (a) initial charge−discharge profiles; (b) cycling performances at a current density of 20 mA g^{-1} (30 °C); (c) rate capabilities; and (d) Nyquist plots after 30 charge/discharge cycles in charging state for the samples K900 and N900. Inset of Figure 4a represents the dQ/dV curves calculated from the charging profiles of samples K900 and N900. The standard deviations of capacity values in panel c are calculated by measuring 3−5 cells at each rate.
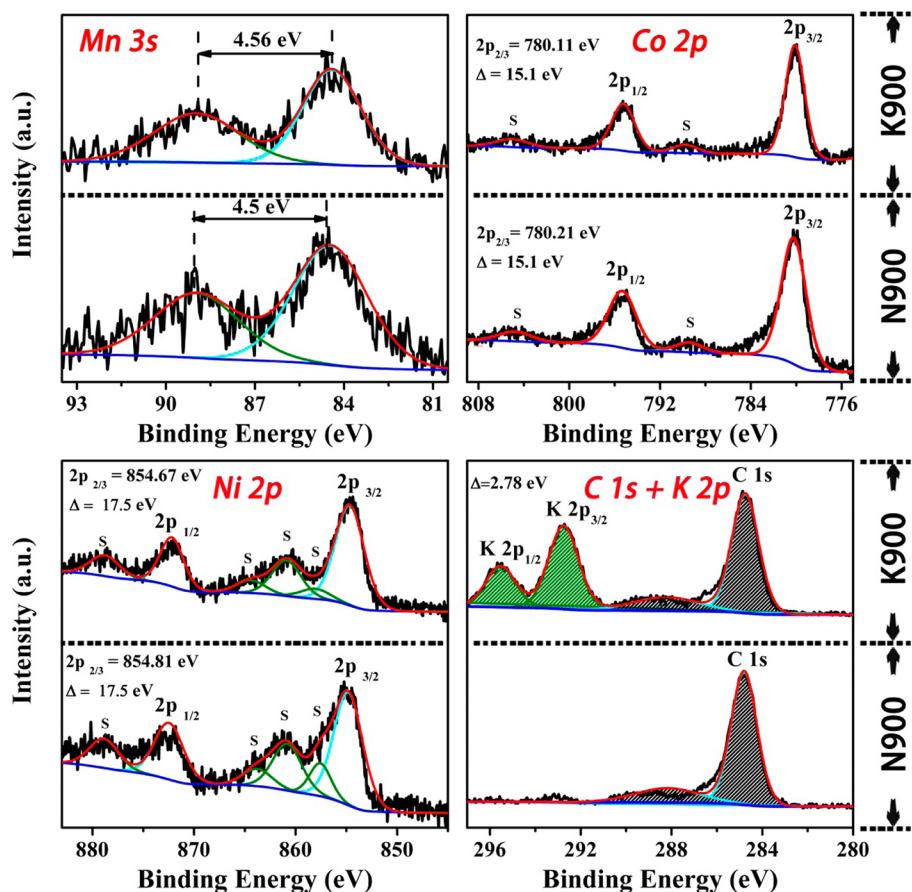
Figure 5. XPS spectra of Mn 3s, Co 2p, Ni 2p, C 1s, and K 2p for samples K900 and N900, with the experimental data (black line), calculated pattern (red line), background (blue line), and fitted peaks (green and cyan lines).

almost the same charging capacity at ca. 400 mA h g^{-1}. It is well-known that Li-rich oxides usually suffer from large irreversible capacity losses (ICL) during the first cycle, and Li$_2$O leaching because of Li$_2$MnO$_3$ activation above ca. 4.5 V is believed to be the main source of ICL. To explore whether K doping has any impacts on this process, dQ/dV plots are calculated. The sharp peak at 4.5 V is ascribed to Li$_2$MnO$_3$ activation. K doped sample has a slightly lower intensity than the K-free one (inset of Figure 4a), indicating a slightly suppressed oxygen loss after K doping. The discharge capacity for N900 and K900 was 302 and 315 mA h g^{-1}, respectively. The columbic efficiency is calculated based on the first charge/ discharge capacities, which gives a columbic efficiency of 77% for K900 higher than 74% for N900. Consequently, ICL is suppressed for K900, consistent with the reports elsewhere on Na-doping.[25,26]

Cycling stability and rate capability of samples K900 and N900 are compared in Figure 4b, c. Sample N900 exhibited a serious capacity fade: its capacity retention is only 81% (Figure 4b), which is lower than 91% for sample K900. When current densities increased from 100 to 1000 mA g^{-1}, K900 released large capacities of 252.3 ± 6.6, 233.0 ± 6.9, and 197.0 ± 4.4 mA h g^{-1}, respectively. Contrarily, N900 delivered capacities of 236.4 ± 4.5, 224.1 ± 8.1, and 142.3 ± 10.4 mA h g^{-1} at the corresponding rates, indicating an inferior rate capability for the K-free sample (Figure 4c). Figure 4d shows their electro-chemical impedance data with the fitted kinetic parameters listed in Table S1 in the Supporting Information. A much reduced surface and charge-transfer resistance is observed for

K900 at the end of cycling. Li$^+$ diffusion coefficient is calculated using the EIS data with the method reported elsewhere[34,35] to detect the different Li$^+$ diffusion kinetics. The diffusion coefficient of K900 at fully charged state is calculated to be 1.26×10^{-15} cm^2 s^{-1}, which compares to that of 7.01×10^{-16} cm^2 s^{-1} for N900. It is thus clear that K doping facilitates Li$^+$ diffusion.

It is unambiguous that K900 embodies much better electrochemical performance than N900. Preliminary conclusion could be made: doped potassium play a positive role in Li-rich layered oxide. In the following, detailed investigations were conducted to uncover the difference between potassium-doped and potassium-free samples.

1. Influence of Potassium's Incorporation on Pristine Materials. What is the main reason for the big difference in electrochemical performance between samples K900 and N900? It is well-known that in the layered LiMO$_2$ cathode, transition metal elements Mn, Co, and Ni govern the capacity, rate, and cycling performance. Therefore, the relative contents of transition metal element in the samples K900 and N900 were first determined by ICP. The test results showed that Li, Mn, Co, and Ni contents were 8.98, 33.86, 9.61, and 9.49 wt % with a relative error of ±2%, for sample K900, which are comparable to the corresponding values of 9.18, 35, 9.41, and 9.22 wt % for sample N900. K content was 0.55 wt % for sample K900. According to the test values, the deduced formula could be obtained, as listed in Table 1. It is obvious that both samples exhibit a similar content of transition metals. Second, examining the particle size and morphology is necessary,
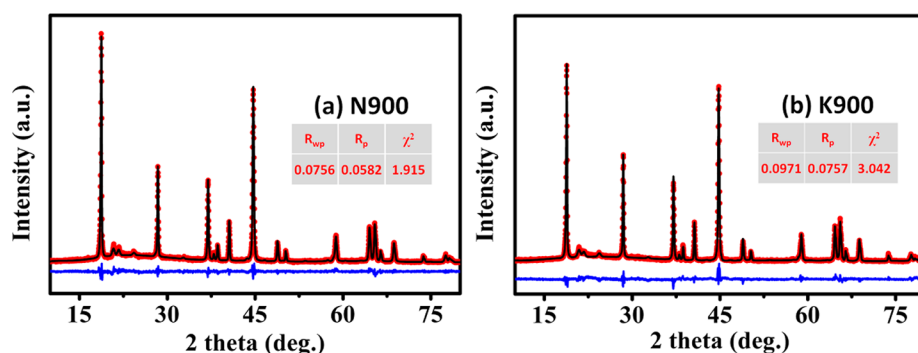
Figure 6. XRD patterns of (a) K900 and (b) N900, with the experimental data (red dots), calculated pattern (black line) and difference curve (blue line). Inset table displays refinement parameters (GSAS software). The refinement was conducted on the base of both trigonal ($R\bar{3}m$) and monoclinic ($C2/m$) phases.

because particle size and morphology are thought to have an important influence on electrochemical performance. As displayed in Figure S8 in the Supporting Information, N900 and K900 have very similar particle morphology and size distribution. Therefore, we could eliminate the effect of particle size and morphology.

Next, we examined the valence states of transition metals in both samples by XPS. The core level photoelectron peaks of Mn 3s, Co 2p, Ni 2p, C 1s, K 2p, and Mn 2p are shown in Figure 5 and Figure S9 in the Supporting Information. The peak positions of Mn 3s, Mn 2p, Co 2p, and Ni 2p are very close to those reported in references,[8,36−40] indicating the presence of Mn^{4+}, Co^{3+}, and Ni^{2+} for both pristine K900 and N900. The notable difference could be found in the binding energy region from 280 to 297 eV: in addition to the C 1s level observed at 284.8 and 288.2 eV for both samples, sample K900 exhibits two strong peaks at higher binding energy (>290 eV), as highlighted by the green shadow in Figure 5. These two peaks could well be assigned to K $2p_{3/2}$ and $2p_{1/2}$.[41−43] The observation of spin−orbital levels gives a direct evidence for the existence of potassium in K900. The almost identical photoelectron signals observed for transition metal ions in both K900 and N900 suggest that valence state is not a crucial factor for enhancing the electrochemical performance of sample K900.

Lattice dimension of the layered oxides is another factor that should be considered. XRD refinements based on both trigonal ($R\bar{3}m$) and monoclinic ($C2/m$) phases for samples K900 and N900 (Figure 6) were further performed to investigate the effect of potassium's incorporation on pristine structure. The obtained lattice parameters of $R\bar{3}m$ phase and $C2/m$ phases are listed in Table 1 and Table S2 in the Supporting Information, respectively. It is interesting that introducing a small amount of potassium in sample K900 results in a slight lattice contraction for both phases, whereas the c/a value of $R\bar{3}m$ phase was maintained. This observation is different with previous reports for Na^+-doped Li-rich oxides.[25] By considering the larger K^+ ions (1.38 Å) in ideal 6-coordination and its concentration of ca. 1.13% (molar ratio), it can be calculated that the effective ionic radius is 0.7669 Å for the ions at 3b sites, slightly larger than that of 0.76 Å for Li^+, the lattice parameter c should be enlarged after doping. But when considering the possibility of deviation from the ideal coordination, lattice contraction is understandable, because this deviation would give rise to a lattice distortion and strain in the K^+-related local structure. These distortion and strain might lead to a slight lattice

constriction. Unfortunately, X-ray diffraction techniques can only provide the information on the integrated crystal structure, and is not sensitive to the local atomic environment. Nevertheless, though lattice parameter c is contracted, Li slab space (I_{LiO2}) is calculated to be enlarged for K900 (Table 1), in agreement with Na-doped samples. The contrary variations of c and I_{LiO2} are the evidence for the presence of K in Li slab rather than TM slab. When considering that K ions reside in the diffusion channel of Li layers, some hindrance on Li diffusion rate should exist. One has to note that the dopant level is relatively low, and thus the existence of K ions will not totally block the diffusion path. This may explain why the hindrance is not obvious. On the other hand, the calculation of interslab thickness of LiO2 (I_{LiO2}) indicates that K doped samples have a larger I_{LiO2}. Previous investigations[30,44,45] have shown that larger I_{LiO2} reduces an activation barrier for Li hopping and thus facilitates Li migration. It appears that the latter effect plays a leading role in Li diffusion. All these may explain the improved rate capability and the larger Li diffusion coefficient of K900.

Taking all together, it seems that the doped potassium did not give rise to the variation of pristine materials' grain size and chemical valence state. The enlarged interslab space thickness I_{LiO2} is only responsible for the enhanced rate capability of K900 but cannot account for the enhanced cycling stability. Therefore, detailed studies about the charge/discharge processes are expected to reveal the intrinsic variations upon cycling.

2. Influence of Potassium's Incorporation on Cycling Processes. Discharge profiles at a rate of 20 mA g^{-1} are displayed in Figure 7. Prior to discharge, the cells were relaxed for 5 min at charged-state (4.8 V). In fact, the effect of polarization is very common for Li-rich cathodes, which leads to the open-circuit voltage decay and thus the starting discharge voltage is usually lower than 4.8 V. The reducing value in voltage is a criterion for evaluating the effect of polarization. As can be seen from the histograms in Figure 7, the starting discharge voltage for the initial cycle are a little larger than 4.6 V for both samples. In the following cycles, this voltage remained quite consistent with first cycle for K900. But for N900, there was a notable decrease. This implies a larger polarization for the potassium-free sample.

Importantly, a much faster voltage decline can be readily observed for N900 in Figure 7, accompanying rapid capacity fading. dQ/dV plots were calculated from numerical data observed in discharge profiles of various cycles to further reveal this voltage decay, as displayed in Figure 8. In the discharging
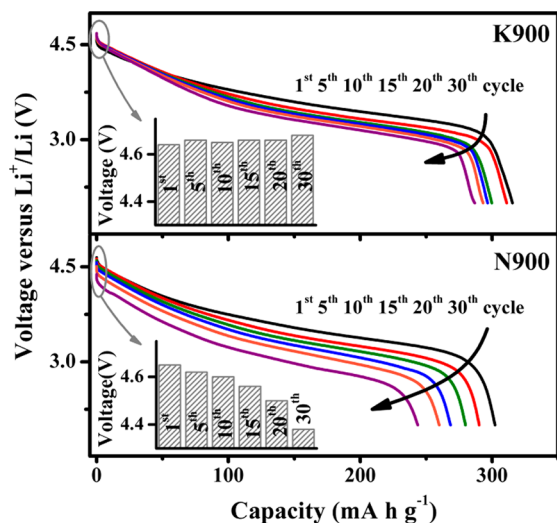
10335

dx.doi.org/10.1021/am5017649 | *ACS Appl. Mater. Interfaces* 2014, 6, 10330−10341

Figure 7. Discharge curves of 1, 5, 10, 15, 20, and 30 cycles at current density of 20 mA g^{-1} for samples K900 and N900. Inset histogram shows the variation trend of starting discharge voltage after different cycles.

curves, there are mainly three electrochemical processes, noted as R_{e1} around 4.5 V, R_{e2} at 3.7 V, and R_{e3} lower than 3.5 V. It was documented that R_{e1} is ascribed to Li occupation within tetrahedral sites; R_{e2} is related to Li occupation within octahedral sites accompanied by Ni$^{+4/+3/+2}$ and Co$^{4+/3+}$ redox couples, which is overlapped within a broad peak in the subsequent cycles; R_{e3} is associated with Mn^{4+}/Mn^{3+} redox related to Li occupation within octahedral sites.[5] Clearly, R_{e3} for N900 shifts continuously toward lower potential upon cycling. At 15th cycle (Figure 8d), a swelling at ca. 2.8 V can be

observed, which indicates the presence of spinel phase in the host structure. A continued growth of spinel phase results in the broadening of this reduction peak at 20th cycle (Figure 8e) and eventually the sharp peak at 2.84 V in Figure 8f. Similar peak at 2.84 V is usually linked to the spinel phase.[5,14,19,26] Comparatively, for K900, no remarkable change at 2.8 V was observed, implying the absence of spinel phase during the cycling process. To verify this point, ex situ XRD patterns of both K900 and N900 at the end of cycling were collected and compared with pristine materials.

Figure 9 displays the ex situ XRD patterns before and after cycling. It can be found that the short-ranged peaks between 20 and 25° disappeared because of the activation of the Li$_2$MnO$_3$ component. Sample K900 at the end of cycling still gave a sharp peak (003), and the separation of the doublet (018)/(110) remained evident, indicating no severe change of the host layered structure during cycling. Comparatively, for sample N900, (018)/(110) splitting is much weakened, suggesting a damaged layered structure. In particular, the (003) peak is broadened, and some impurities appear for sample N900 after 30 cycles, which is believed to be associated with the spinel variant.[25,26,47]

In general, ex situ XRD combined with the electrochemical analysis confirms that an evident spinel growth does exist in N900 but not in K900. Different structural evolution upon cycling is supposed to give rise to different kinetics in electrode process. Thus, electrochemical impedance spectroscopy (EIS) measurements were then performed to verify the different structural stability.

Nyquist plots for K900 and N900 at selected cycles are shown in Figure 10. All data could be well fitted to the equivalent circuit shown in the insets. The corresponding resistance parameters are illustrated in Figure 10c, d (numerical
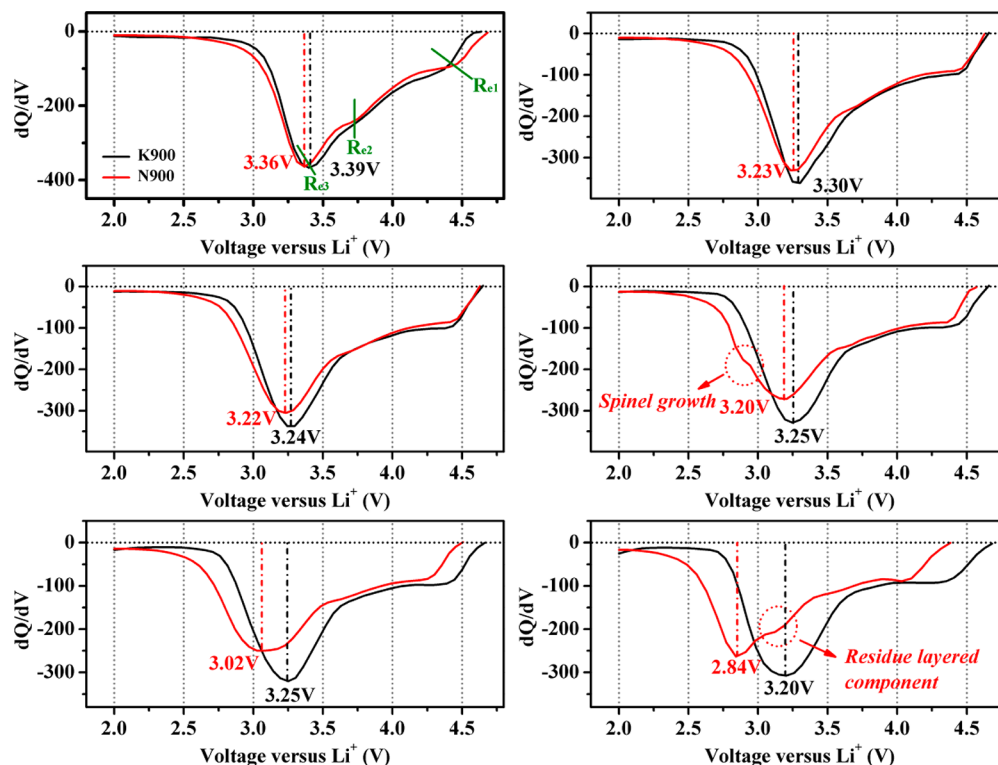

Figure 8. dQ/dV profiles calculated from numerical data observed after (a) 1st, (b) 5th, (c) 10th, (d) 15th, (e) 20th, and (f) 30th cycle at 20 mA g^{-1}.
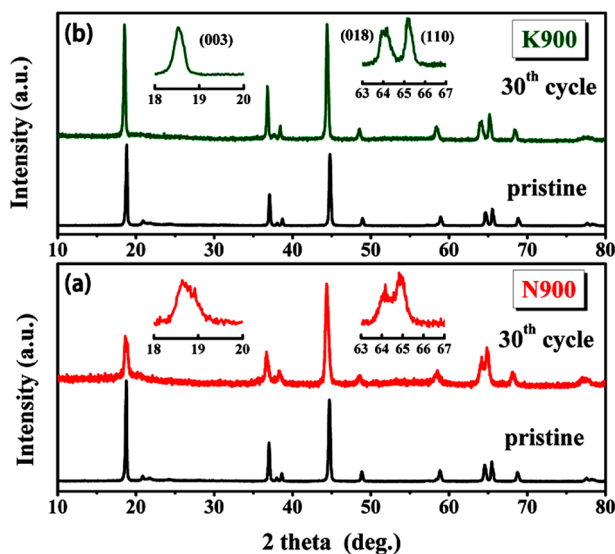
Figure 9. Ex situ XRD patterns for the samples: (a) N900 and (b) K900 before and after 30 cycles.

data can be found in Table S3 in the Supporting Information). In this model, C_{sl} and C_{dl} are the capacitances of SEI film and double layer, respectively; W is the Warburg impedance directly related to lithium ion diffusion. The total resistance (the red column in Figure 10b) is the sum of R_e (internal resistance), R_{sf} (resistance of SEI film) and R_{ct} (the charge transfer resistance).[48,49]

The variation in kinetic parameters is closely related to the inside transformations, and is also responsible for the cycling stability. By monitoring both samples, it is found that both samples have similar variation trends in R_e and R_{sf}: R_e remains almost unchanged, whereas R_{sf} has a clear growth upon cycling possibly due to the growth of SEI film. Further comparison in the R_{sf} values (see Table S3 in the Supporting Information) reveals a reduced R_{sf} for K900 at first cycle. This is more evident with cycling. The doped K^+ is supposed to have an indirect influence on surface kinetics (see detailed discussion in the Supporting Information). Here, we care about the variation trend of R_{ct}, which is more relevant to the inside structural transformation. R_{ct} of N900 reaches to the lowest at first cycle. In the subsequent cycles, R_{ct} kept increasing significantly, implying a continuous structural evolution upon cycling. On the contrary, R_{ct} of K900 reaches to the highest at first cycle. As is widely acknowledged, Li_2MnO_3 is an electrochemically inert component with large resistance,[2,50−52] although it can be activated when charged above 4.5 V by leaching Li_2O to yield a MnO_2-like structure,[2,51] the whole Li_2MnO_3 can hardly be consumed for just one cycle and residual Li_2MnO_3 resulted in the high resistance for the first cycle. Further activation of Li_2MnO_3 is required, accompanied by the reduction of resistance and slight increase of capacity upon cycling in the beginning cycles (as observed in Figure 2c). This difference for N900 could be due to K^+ ions' influence on the activation process of Li_2MnO_3, as discussed earlier. As cycling continues, R_{ct} picks up a little from fifth to 15th cycle and finally attains a constant value, suggesting that the transformation in the cathode finished.
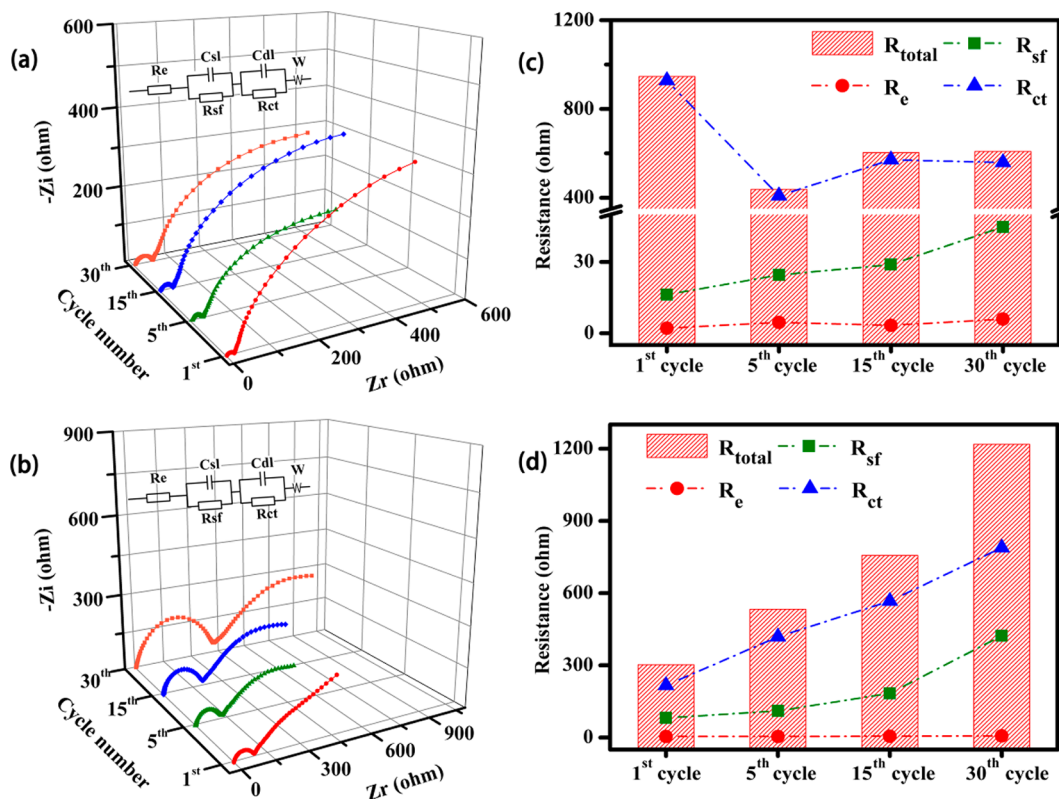

Figure 10. Nyquist plots and corresponding fitted parameters of the samples: (a, c) K900 and (b, d) N900 in charged state (4.8 V) after 1, 5, 15, and 30 charge/discharge cycles between 4.8 and 2.0 V. Insets in Figure 10a and Figure 10b are the equivalent circuits for data fitting. The cells were first charged to 4.8 V at a rate of 100 mA g^{-1} and then held at 4.8 V until current density decreased to 20 mA g^{-1} prior to being used for the test.
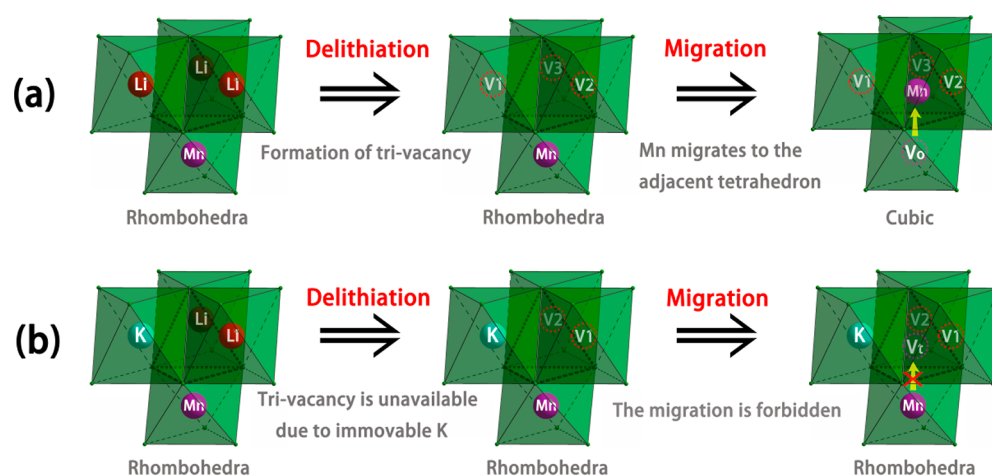
Figure 11. Schematic diagrams of the phase evolution routes for (a) potassium-free and (b) potassium-doped insertion oxides. It was built on O3 layered model with unrealistic radii ratios. Vertexes of the octahedrons are oxygen atoms. V_1, V_2 and V_3 stand for vacancies in lithium layer; V_t stands for tetrahedral vacancy and V_o for octahedral vacancy.

Stable structure of K900 is confirmed by EIS analysis. Combining with the investigations into electrochemistry and ex situ XRD results, the superior cycling performances for the prepared LLOs could be well understood. Herein an important fact should be highlighted again: in situ doped potassium mitigated the spinel formation upon cycling and stabilized the layered host structure. Interestingly, He et al.[25] recently reported that spinel growth could also be suppressed by Na doping. This gave us a thought-provoking speculation that alkali ions are effective in inhibiting phase transition in layered Li-rich oxides. How can such a process occur? To answer this question, we must mention a similar work in ref 26. To explain the inhibiting role of Na ions for the phase transition in LLOs, the authors suggested that (1) a proportion of doped Na ions could exchange with Li upon charging; (2) Ni–O and Ni–M–M bond were enlarged, thereby leading to volume expansion for Na doped sample; (3) some additional TM rearrangement occurred after the charging process. On the basis of these results, they further deduced that after a proportion of Na was exchanged with Li, transition metal (possibly Ni^{3+}) would migrate to this Na depleted sites, which could protect it against conversion to spinel structure.

The explanation given by Ates et al.[26] is reasonable, but it is still an ambiguous conclusion on the basis of the following considerations: (1) Ni^{3+} migration is only an assumption, different from the reversible migration of Mn into lithium layer from Li_2MnO_3 at early charge–discharging stage that was directly observed by STEM;[53] (2) the effect of remaining Na in the lithium layer, responsible for a higher conductivity, is not considered yet. In addition to the migrated ions, the barrier that governs the unhappened phase transition from layered to spinel structure should also be explicated; (3) because of a relatively larger ionic radius and lower electronegativity, K^+ ion should show different behaviors from Na^+ in migration ability as well as lattice size change. So, we would like to share our perspectives in explaining this inhibited phase transition.

3.3. Understanding Spinel Growth Mitigated by Alkali Ion Doping. From a thermodynamic point of view, spinel is more stable than O3 phase observed for $LiMnO_2$-like oxides at partial delithiation.[24,54] The doped alkali ion could hardly reverse the free energy of the integrated structure to relief this thermodynamic driving force. Nevertheless, on the other hand,

it can be understood from the viewpoint of kinetics, i.e. the transition from O3 to spinel structure could be inhibited by reducing the kinetics rate of transition metals (e.g., Mn) migration. This should be closely related to the crystallography environment. The following two considerations are essential.

1. Inhibition of Trivacancy Formation. First, two facts should be mentioned: the activation of Li_2MnO_3 gives a MnO_2-like structure and this produces an expected $LiMnO_2$ (layered O3 structure) after intercalation.[2,51] As well-known, a crucial step in the structure transition from layered structure (rhombohedral symmetry) to the spinel variant (cubic symmetry) is the migration of transition metal ions from octahedral coordination to adjacent tetrahedral sites. This migration is accessible only if the three adjacent octahedral sites in the lithium layer are vacant, thus forming a trivacancy at some degree of deintercalation upon charging,[24,55] as illustrated in Figure 11a. For alkali-doped layered oxides, partial doped ions, especially K^+ ions, will not migrate out from the lattice[26] and would act as fixed pillars in lithium layers. In that case, formation of trivacancies in lithium layer is suppressed, and the transition from layered to spinel structure is inhibited consequently (see Figure 11b).

2. Steric Hindrance Originated from Large Ion Radius. Furthermore, the inhibition of spinel growth by alkali ion doping could also be understood when taking ion radius into account. It is widely known that there are two types of sites (interstitial voids) in the cubic close-packed oxygen array, i.e. one tetrahedron site and one octahedron site. For a typical spinel structure AB_2O_4, cations A and B occupy the two kinds of sites, respectively. Take $LiMn_2O_4$ for example, Li occupies tetrahedron site (8a site) and Mn occupies octahedron site (16d site) to give a cation distribution of $[A]_{8a}[B_2]_{16d}O_4$. The largest atom radii for cations A and B that the oxygen skeleton could accommodate is determined when considering the lattice parameter a and oxygen parameter u. The upper limit represents the radius of inscribed sphere within the polyhedrons formed by nearest oxygen atoms. So it is easy to understand that large cations are hard to form spinel structure within a fixed oxygen framework, and vice versa. K^+ and Na^+ ionic radii are much larger than lithium's. Therefore, for potassium and sodium doped Li-rich oxides, transition from layered structure to spinel variant is not supported because of

steric hindrance in the Na/K-containing domains, unless significant lattice distortion occurs. This could be complemented by that $Na_{0.5}MO_2$ have more robust structures than $Li_{0.5}MO_2$ and transition from layered to spinel structure cannot occur in the Na compound by first principles calculations.[54] Nevertheless, it does not mean that the layer to spinel transformation is absolutely inhibited for the Na/K-doped LLOs, because in the Li-rich Mn-based parent compound with majority of Li atoms, the thermodynamic driving force on the transformation always exists for the Li-related phases. Assuming that the doped Na/K ions uniformly distributed in the host structure of the doped samples, one can expect an overall hindrance existing in the host structure, and thus mitigates the transformation due to kinetic factors. But structure distortion would occur during long-term cycling because of multiple factors e.g. Jahn–Teller distortion arose from the appearance of Mn^{3+}. Mn^{3+} ions are also well-known to feed a charge-disproportionation reaction to give Mn^{2+} ions, which have the preference for tetrahedral sites over octahedral sites to form spinel variant.[24] Taken all together, spniel phase would finally occur for doped samples in subsequent cycles. But when comparing to Na/K-free sample, this process is obviously postponed.

In the end, it should be mentioned that the long-term confusion in the accurate mechanism of layered-spinel intergrowth in Li-rich oxides is under ongoing research.[53] Correlated studies are being constantly reported worldwide.[3,5,9–18] Herein, we proposed a hypothesis from kinetic consideration based on crystallography. Although we strongly believe that this is theoretically possible, experimental proof is indispensible. Further investigation regarding the influence of K concentration and verifying the hypothesis is under way.

CONCLUSION

High-performance Li-rich layered oxides with rechargeable capacity over 310 mA h g^{-1} were prepared using potassium-containing α-MnO_2 as starting material. Within this facile synthesis route, potassium was in situ doped into the cathode oxide. For the first time, we found that incorporation of potassium about 0.013 mol per formula weight significantly improved the cycling performance, and after 110 cycles, the discharge capacity at 20 mA g^{-1} was as high as 267 mA h g^{-1} with a capacity retention of 85% relative to the first cycle. The superior cycling performance thus observed is supposed to be related to the doping of potassium that effectively mitigated the transition from layered structure to spinel variant. The doped potassium might weaken the formation of trivacancies in lithium layer and Mn migration to form spinel structure; besides, the large ion radius of potassium can possibly aggravate steric hindrance for spinel growth. Therefore, our observations on potassium's effect along with recent literature works on sodium's impact may provide a vital hint for inhibiting the undesired layered-spinel intergrowth with alkali ion doping and for breakthroughs in today's state-of-art Li-ion batteries.

ASSOCIATED CONTENT

ⓢ Supporting Information

Synthesis detail, experimental data of K800, complementary electrochemical performances, morphological comparison and numerical fitted data for EIS measurements, refined lattice parameters of the $C2/m$ phase. This material is available free of charge via the Internet at http://pubs.acs.org/.

AUTHOR INFORMATION

Corresponding Author

*E-mail: lipingli@fjirsm.ac.cn. Fax: (+) 86-591-83702122.

Notes

The authors declare no competing financial interest.

ACKNOWLEDGMENTS

REFERENCES

(1) Robertson, A. D.; Bruce, P. G. The Origin of Electrochemical Activity in Li_2MnO_3. *Chem. Commun.* **2002**, 2790−2791.

(2) Thackeray, M. M.; Kang, S.-H.; Johnson, C. S.; Vaughey, J. T.; Benedek, R.; Hackney, S. A. Li_2MnO_3-Stabilized $LiMO_2$ (M = Mn, Ni, Co) Electrodes for Lithium-Ion Batteries. *J. Mater. Chem.* **2007**, 17, 3053−3272.

(3) Yabuuchi, N.; Yoshii, K.; Myung, S. T.; Nakai, I.; Komaba, S. Detailed Studies of a High-Capacity Electrode Material for Rechargeable Batteries, Li_2MnO_3-$LiCo_{1/3}Ni_{1/3}Mn_{1/3}O_2$. *J. Am. Chem. Soc.* **2011**, 133, 4404−4419.

(4) Yu, H. J.; Zhou, H. S. High-Energy Cathode Materials (Li_2MnO3-$LiMO_2$) for Lithium-Ion Batteries. *J. Phys. Chem. Lett.* **2013**, 4, 1268−1280.

(5) Song, B.; Liu, H.; Liu, Z.; Xiao, P.; Lai, M. O.; Lu, L. High Rate Capability Caused by Surface Cubic Spinels in Li-Rich Layer-Structured Cathodes for Li-Ion Batteries. *Sci. Rep.* **2013**, 3, 3094.

(6) Liu, J. L.; Chen, L.; Hou, M. Y.; Wang, F.; Che, R. C.; Xia, Y. Y. General Synthesis of $xLi_2MnO_3\cdot(1-x)LiMn_{1/3}Ni_{1/3}Co_{1/3}O_2$ Nanomaterials by a Molten-Salt Method: towards a High Capacity and High Power Cathode for Rechargeable Lithium Batteries. *J. Mater. Chem.* **2012**, 22, 25380−25387.

(7) Luo, D.; Li, G.; Guan, X.; Yu, C.; Zheng, J.; Zhang, X.; Li, L. Novel Synthesis of $Li_{1.2}Mn_{0.4}Co_{0.4}O_2$ with an Excellent Eectrochemical Performance from −10.4 to 45.4 °C. *J. Mater. Chem. A* **2013**, 1, 1220−1227.

(8) Fu, C.; Li, G.; Luo, D.; Zheng, J.; Li, L. Gel-Combustion Synthesis of $Li_{1.2}Mn_{0.4}Co_{0.4}O_2$ Composites with High Capacity and Superior Rate Capability for Lithium-Ion Batteries. *J. Mater. Chem. A* **2014**, 2, 1471−1483.

(9) Shi, S. J.; Tu, J. P.; Tang, Y. Y.; Yu, Y. X.; Zhang, Y. Q.; Wang, X. L.; Gu, C. D. Combustion Synthesis and Electrochemical Performance of $Li[Li_{0.2}Mn_{0.54}Ni_{0.13}Co_{0.13}]O_2$ with Improved Rate Capability. *J. Power Sources* **2013**, 228, 14−23.

(10) Shi, S. J.; Tu, J. P.; Tang, Y. Y.; Zhang, Y. Q.; Wang, X. L.; Gu, C. D. Preparation and Characterization of Macroporous $Li_{1.2}Mn_{0.54}Ni_{0.13}Co_{0.13}O_2$ Cathode Material for Lithium-Ion Batteries via Aerogel Template. *J. Power Sources* **2013**, 240, 140−148.

(11) West, W. C.; Soler, J.; Ratnakumar, B. V. Preparation of High Quality Layered-Layered Composite Li_2MnO_3-$LiMO_2$ (M = Ni, Mn, Co) Li-Ion Cathodes by a Ball Milling-Annealing Process. *J. Power Sources* **2012**, 204, 200−204.

(12) Lee, J.; Urban, A.; Li, X.; Su, D.; Hautier, G.; Ceder, G. Unlocking the Potential of Cation-Disordered Oxides for Rechargeable Lithium Batteries. *Science* **2014**, 343, 519−522.

(13) Gu, M.; Genc, A.; Belharouak, I.; Wang, D.; Amine, K.; Thevuthasan, S.; Baer, D. R.; Zhang, J.-G.; Browning, N. D.; Liu, J.; Wang, C. Nanoscale Phase Separation, Cation Ordering, and Surface Chemistry in Pristine $Li_{1.2}Ni_{0.2}Mn_{0.6}O_2$ for Li-Ion Batteries. *Chem. Mater.* **2013**, 25, 2319−2326.

(14) Gu, M.; Belharouak, I.; Zheng, J.; Wu, H.; Xiao, J.; Genc, A.; Amine, K.; Thevuthasan, S.; Baer, D. R.; Zhang, J.-G. Formation of the Spinel Phase in the Layered Composite Cathode Used in Li-Ion Batteries. *ACS Nano* **2012**, 7, 760−767.

10339

dx.doi.org/10.1021/am5017649 | *ACS Appl. Mater. Interfaces* 2014, 6, 10330−10341

(15) Qiu, S.; Chen, Z.; Pei, F.; Wu, F.; Wu, Y.; Ai, X.; Yang, H.; Cao, Y. Synthesis of Monoclinic $Li[Li_{0.2}Mn_{0.54}Ni_{0.13}Co_{0.13}]O_2$ Nanoparticles by a Layered-Template Route for High-Performance Li-Ion Batteries. *Eur. J. Inorg. Chem.* **2013**, *2013*, 2887–2892.

(16) Xu, B.; Fell, C. R.; Chi, M.; Meng, Y. S. Identifying Surface Structural Changes in Layered Li-Excess Nickel Manganese Oxides in High Voltage Lithium Ion Batteries: A joint Experimental and Theoretical Study. *Energy Environ. Sci.* **2011**, *4*, 2223–2233.

(17) Song, B.; Liu, Z.; Lai, M. O.; Lu, L. Structural Evolution and the Capacity Fade Mechanism upon Long-Term Cycling in Li-Rich Cathode Material. *Phys. Chem. Chem. Phys.* **2012**, *14*, 12875–12883.

(18) Mohanty, D.; Sefat, A. S.; Kalnaus, S.; Li, J.; Meisner, R. A.; Payzant, E. A.; Abraham, D. P.; Wood, D. L.; Daniel, C. Investigating Phase Transformation in the $Li_{1.2}Co_{0.1}Mn_{0.55}Ni_{0.15}O_2$ Lithium-Ion Battery Cathode during High-Voltage Hold (4.5 V) via Magnetic, X-ray Diffraction and Electron Microscopy Studies. *J. Mater. Chem. A* **2013**, *1*, 6249–6261.

(19) Lee, E.-S.; Manthiram, A. Smart Design of Lithium-Rich Layered Oxide Cathode Compositions with Suppressed Voltage Decay. *J. Mater. Chem. A* **2014**, *2*, 3932–3939.

(20) Zheng, J.; Gu, M.; Xiao, J.; Zuo, P.; Wang, C.; Zhang, J. G. Corrosion/Fragmentation of Layered Composite Cathode and Related Capacity/Voltage Fading during Cycling Process. *Nano Lett.* **2013**, *13*, 3824–30.

(21) Armstrong, A. R.; Holzapfel, M.; Novak, P.; Johnson, C. S.; Kang, S. H.; Thackeray, M. M.; Bruce, P. G. Demonstrating Oxygen Loss and Associated Structural Reorganization in the Lithium Battery Cathode $Li[Ni_{0.2}Li_{0.2}Mn_{0.6}]O_2$. *J. Am. Chem. Soc.* **2006**, *128*, 8694–8698.

(22) Lu, Z.; Beaulieu, L.; Donaberger, R.; Thomas, C.; Dahn, J. Synthesis, Structure, and Electrochemical Behavior of Li-$[Ni_xLi_{1/3-2x/3}Mn_{2/3-x/3}]O_2$. *J. Electrochem. Soc.* **2002**, *149*, A778–A791.

(23) Denis, Y.; Yanagida, K. Structural Analysis of Li_2MnO_3 and Related Li-Mn-O Materials. *J. Electrochem. Soc.* **2011**, *158*, A1015–A1022.

(24) Reed, J.; Ceder, G.; Van Der Ven, A. Layered-to-Spinel Phase Transition in Li_xMnO_2. *Electrochem. Solid-State Lett.* **2001**, *4*, A78–A81.

(25) He, W.; Yuan, D.; Qian, J.; Ai, X.; Yang, H.; Cao, Y. Enhanced High-Rate Capability and Cycling Stability of Na-Stabilized Layered $Li_{1.2}[Co_{0.13}Ni_{0.13}Mn_{0.54}]O_2$ Cathode Material. *J. Mater. Chem. A* **2013**, *1*, 11397–11403.

(26) Ates, M. N.; Jia, Q. Y.; Shah, A.; Busnaina, A.; Mukerjee, S.; Abraham, K. M. Mitigation of Layered to Spinel Conversion of a Li-Rich Layered Metal Oxide Cathode Material for Li-Ion Batteries. *J. Electrochem. Soc.* **2014**, *161*, A290–A301.

(27) He, X.; Yang, M.; Ni, P.; Li, Y.; Liu, Z.-H. Rapid Synthesis of Hollow Structured MnO_2 Microspheres and Their Capacitance. *Colloids Surf., A* **2010**, *363*, 64–70.

(28) Fang, H.; Li, L.; Yang, Y.; Yan, G.; Li, G. Low-Temperature Synthesis of Highly Crystallized $LiMn_2O_4$ from Alpha Manganese Dioxide Nanorods. *J. Power Sources* **2008**, *184*, 494–497.

(29) Toby, B. H. EXPGUI, A Graphical User Interface for GSAS. *J. Appl. Crystallogr.* **2001**, *34*, 210–213.

(30) Song, B.; Lai, M. O.; Lu, L. Influence of Ru Substitution on Li-rich $0.55Li_2MnO_3·0.45LiNi_{1/3}Co_{1/3}Mn_{1/3}O_2$ Cathode for Li-Ion Batteries. *Electrochim. Acta* **2012**, *80*, 187–195.

(31) Koga, H.; Croguennec, L.; Menetrier, M.; Douhil, K.; Belin, S.; Bourgeois, L.; Suard, E.; Weill, F.; Delmas, C. Reversible Oxygen Participation to the Redox Processes Revealed for $Li_{1.20}Mn_{0.54}Co_{0.13}Ni_{0.13}O_2$. *J. Electrochem. Soc.* **2013**, *160*, A786–A792.

(32) Tompsett, D. A.; Islam, M. S. Electrochemistry of Hollandite α-MnO_2: Li-Ion and Na-Ion Insertion and Li_2O Incorporation. *Chem. Mater.* **2013**, *25*, 2515–2526.

(33) Huang, X.; Lv, D.; Yue, H.; Attia, A.; Yang, Y. Controllable Synthesis of Alpha- and Beta-MnO_2: Cationic Effect on Hydrothermal Crystallization. *Nanotechnology* **2008**, *19*, 225606.

(34) Cao, Q.; Zhang, H.; Wang, G.; Xia, Q.; Wu, Y.; Wu, H. A Novel Carbon-Coated $LiCoO_2$ as Cathode Material for Lithium Ion Battery. *Electrochem. Commun.* **2007**, *9*, 1228–1232.

(35) Luo, D.; Li, G.; Fu, C.; Zheng, J.; Fan, J.; Li, Q.; Li, L. A New Spinel-Layered Li-Rich Microsphere as a High-Rate Cathode Material for Li-Ion Batteries. *Adv. Energy Mater.* **2014**, DOI: 10.1002/aenm.201400062.

(36) Yu, C.; Guan, X.; Li, G.; Zheng, J.; Li, L. A Novel Approach to Composite Electrode $0.3Li_2MnO_3$-$0.7LiMn_{1/3}Ni_{1/3}Co_{1/3}O_2$ in Lithium-Ion Batteries with an Anomalous Capacity and Cycling Stability at 45.4°C. *Scr. Mater.* **2012**, *66*, 300–303.

(37) Munakata, F.; Takahashi, H.; Akimune, Y.; Shichi, Y.; Tanimura, M.; Inoue, Y.; Itti, R.; Koyama, Y. Electronic State and Valence Control of $LaCoO_3$: Difference between La-Deficient and Sr-Substituting Effects. *Phys. Rev. B* **1997**, *56*, 979–982.

(38) Ivanova, S.; Zhecheva, E.; Stoyanova, R.; Nihtianova, D.; Wegner, S.; Tzvetkova, P.; Simova, S. High-Voltage $LiNi_{1/2}Mn_{3/2}O_4$ Spinel: Cationic Order and Particle Size Distribution. *J. Phys. Chem. C* **2011**, *115*, 25170–25182.

(39) Fu, C.; Li, G.; Luo, D.; Huang, X.; Zheng, J.; Li, L. One-Step Calcination-Free Synthesis of Multicomponent Spinel Assembled Microspheres for High-Performance Anodes of Li-Ion Batteries: A Case Study of $MnCo_2O_4$. *ACS Appl. Mater. Interfaces* **2014**, *6*, 2439–2449.

(40) Zhang, X.; Luo, D.; Li, G.; Zheng, J.; Yu, C.; Guan, X.; Fu, C.; Huang, X.; Li, L. Self-Adjusted Oxygen-Partial-Pressure Approach to the Improved Electrochemical Performance of Electrode Li-$[Li_{0.14}Mn_{0.47}Ni_{0.25}Co_{0.14}]O_2$ for Lithium-Ion Batteries. *J. Mater. Chem. A* **2013**, *1*, 9721.

(41) Kuch, W.; Schulze, M.; Schnurnberger, W.; Bolwin, K. XPS Lineshape Analysis of Potassium Coadsorbed with Water on Ni (111). *Surf. Sci.* **1993**, *287*, 600–604.

(42) Xiang, M.; Li, D.; Qi, H.; Li, W.; Zhong, B.; Sun, Y. Mixed Alcohols Synthesis from Carbon Monoxide Hydrogenation over Potassium Promoted β-Mo_2C Catalysts. *Fuel* **2007**, *86*, 1298–1303.

(43) Xiang, M.; Li, D.; Li, W.; Zhong, B.; Sun, Y. Potassium and Nickel Doped β-Mo_2C Catalysts for Mixed Alcohols Synthesis via Syngas. *Catal. Commun.* **2007**, *8*, 513–518.

(44) Kang, K.; Meng, Y. S.; Breger, J.; Grey, C. P.; Ceder, G. Electrodes with High Power and High Capacity for Rechargeable Lithium Batteries. *Science* **2006**, *311*, 977–80.

(45) Ceder, G. Opportunities and Challenges for First-Principles Materials Design and Applications to Li Battery Materials. *MRS Bull.* **2011**, *35*, 693–701.

(46) Rougier, A.; Gravereau, P.; Delmas, C. Optimization of the Composition of the $Li_{1-z}Ni_{1+z}O_2$ Electrode Materials: Structural, Magnetic, and Electrochemical Studies. *J. Electrochem. Soc.* **1996**, *143*, 1168–1175.

(47) Ates, M. N.; Mukerjee, S.; Abraham, K. M. A Li-Rich Layered Cathode Material with Enhanced Structural Stability and Rate Capability for Li-Ion Batteries. *J. Electrochem. Soc.* **2014**, *161*, A355–A363.

(48) Yu, C.; Li, G. S.; Guan, X. F.; Zheng, J.; Li, L. P.; Chen, T. W. Composites $Li_2MnO_3·LiMn_{1/3}Ni_{1/3}Co_{1/3}O_2$: Optimized Synthesis and Applications as Advanced High-Voltage Cathode for Batteries Working at Elevated Temperatures. *Electrochim. Acta* **2012**, *81*, 283–291.

(49) Luo, D.; Li, G. S.; Yu, C.; Yang, L. S.; Zheng, J.; Guan, X. F.; Li, L. P. Low-Concentration Donor-Doped $LiCoO_2$ as a High Performance Cathode Material for Li-Ion Batteries to Operate between −10.4 and 45.4 °C. *J. Mater. Chem.* **2012**, *22*, 22233–22241.

(50) He, P.; Yu, H.; Zhou, H. Layered Lithium Transition Metal Oxide Cathodes towards High Energy Lithium-Ion Batteries. *J. Mater. Chem.* **2012**, *22*, 3680–3695.

(51) Thackeray, M. M.; Johnson, C. S.; Vaughey, J. T.; Li, N.; Hackney, S. A. Advances in Manganese-Oxide "Composite" Electrodes for Lithium-Ion Batteries. *J. Mater. Chem.* **2005**, *15*, 2257–2267.

10340

dx.doi.org/10.1021/am5017649 | *ACS Appl. Mater. Interfaces* 2014, 6, 10330–10341

(52) Singh, G.; West, W. C.; Soler, J.; Katiyar, R. S. In Situ Raman Spectroscopy of Layered Solid Solution Li_2MnO_3-$LiMO_2$ (M = Ni, Mn, Co). *J. Power Sources* **2012**, *218*, 34−38.

(53) Wang, R.; He, X.; He, L.; Wang, F.; Xiao, R.; Gu, L.; Li, H.; Chen, L. Atomic Structure of Li_2MnO_3 after Partial Delithiation and Re-Lithiation. *Adv. Energy Mater.* **2013**, *3*, 1358−1367.

(54) Kim, S.; Ma, X.; Ong, S. P.; Ceder, G. A Comparison of Destabilization Mechanisms of the Layered Na_xMO_2 and Li_xMO_2 Compounds upon Alkali De-intercalation. *Phys. Chem. Chem. Phys.* **2012**, *14* (44), 15571−8.

(55) Van Der Ven, A.; Ceder, G. In *Lithium Batteries: Science and Technology*; Nazri, G. A., Pistoia, G., Eds.; Springer: New York, 2009; Chapter 2, pp 71−78.